**Accepted Article Preview: Published ahead of advance online publication**

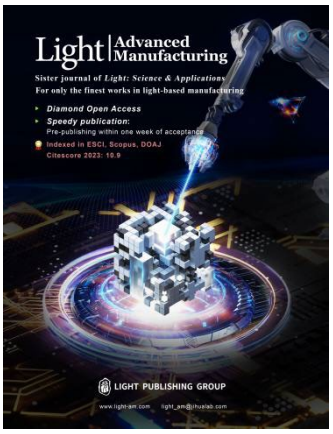


# Host-Engineered Carbon Dot Luminescence: Integration with Nanowires for Photonics

Valeriy M. Kondratev, Andrei A. Ushkov, Maria A. Anikina, Elizaveta P. Karaseva, Ivan A. Kozko, Ekaterina A. Vyacheslavova, Alexander S. Gudovskikh, Vladislav O. Gridchin, Konstantin P. Kotlyar, Alexey Kuznetsov, Viktor V. Zakharov, Maxim A. Rider, Mariia S. Kovova, Talgat Shugabaev, Sergey V. Bazhenov, Stanislav V. Shmakov, Anna O. Orlova, Vladimir V. Fedorov, George E. Cirlin, Ivan S. Mukhin, Vladimir G. Leiman, Alexander V. Syuy, Aleksey V. Arsenin and Alexey D. Bolshakov.

Cite this article as: Valeriy M. Kondratev, Andrei A. Ushkov, Maria A. Anikina, Elizaveta P. Karaseva, Ivan A. Kozko, Ekaterina A. Vyacheslavova, Alexander S. Gudovskikh, Vladislav O. Gridchin, Konstantin P. Kotlyar, Alexey Kuznetsov, Viktor V. Zakharov, Maxim A. Rider, Mariia S. Kovova, Talgat Shugabaev, Sergey V. Bazhenov, Stanislav V. Shmakov, Anna O. Orlova, Vladimir V. Fedorov, George E. Cirlin, Ivan S. Mukhin, Vladimir G. Leiman, Alexander V. Syuy, Aleksey V. Arsenin, Alexey D. Bolshakov. Host-Engineered Carbon Dot Luminescence: Integration with Nanowires for Photonics. *Light: Advanced Manufacturing* accepted article preview 24 April 2026; doi: 10.37188/lam.2026.075



Received 30 January 2026; revised 23 April 2026; accepted 24 April 2026; Accepted article preview online 24 April 2026

# Host-Engineered Carbon Dot Luminescence: Integration with Nanowires for Photonics

**Valeriy M. Kondratev[1,2,*], Andrei A. Ushkov[2], Maria A. Anikina[1,2], Elizaveta P. Karaseva[1,2], Ivan A. Kozko[2], Ekaterina A. Vyacheslavova[1], Alexander S. Gudovskikh[1], Vladislav O. Gridchin[1,6,7], Konstantin P. Kotlyar[1,6,7], Alexey Kuznetsov[2], Viktor V. Zakharov[3], Maxim A. Rider[3], Mariia S. Kovova[3], Talgat Shugabaev[1,6], Sergey V. Bazhenov[2], Stanislav V. Shmakov[1], Anna O. Orlova[3], Vladimir V. Fedorov[1,4], George E. Cirlin[1,6,7], Ivan S. Mukhin[1], Vladimir G. Leiman[2], Alexander V. Syuy[2,5,8], Aleksey V. Arsenin[2,5], Alexey D. Bolshakov[1,2,6,**]**

[1] Alferov University, Khlopina 8/3, Saint Petersburg 194021, Russia

[2] Moscow Center for Advanced Studies, Kulakova str. 20, Moscow, 123592, Russia

[3] International Laboratory "Hybrid Nanostructures for Biomedicine", PhysNano Department ITMO University, Birzhevaya line 14, Saint Petersburg 197101, Russia

[4] Higher School of Engineering Physics, Peter the Great Saint Petersburg Polytechnic University, Politekhnicheskaya 29, Saint Petersburg 195251, Russia

[5] Emerging Technologies Research Center, XPANCEO, Dubai Investment Park 1, Dubai, United Arab Emirates

[6] Faculty of Physics, St. Petersburg State University, Universitetskaya Embankment 7-9, Saint Petersburg 199034, Russia

[7] Institute for Analytical Instrumentation RAS, Saint Petersburg, 190103, Russia

[8] Department of General Physics, Perm National Research Polytechnic University, Perm 614990, Russia.

*phdkondratevvalerii@gmail.com

**bolshakov@live.com

## Abstract

The integration of luminescent nanomaterials into scalable semiconductor platforms is vital for on-chip photonics. This study demonstrates an approach to fabricate fluorescent nanostructures by hybridising carbon dots (CDs) with semiconductor nanowires (NWs) grown on Si. We systematically investigated the photoluminescence of CDs on GaN, GaP, and Si NW hosts and demonstrated the key role of the absorption edge of the host as a practical spectral filter. Our results show that efficient CD excitation is governed by the transparency window of the NW, thereby allowing the precise tailoring of the emission spectrum through rational host selection. This effect has been consistently demonstrated in different materials. By coupling the tuneable chemistry of CDs with the tailored optoelectronics of semiconductor NWs, this study establishes a scalable host–guest architecture for engineering nanoscale light sources to promote applications in integrated photonic circuits and sensing.

**Keywords:** Carbon Dots, Photoluminescence, Nanowires, Host-Engineered Luminescence

## Introduction

Carbon dots (CDs) are a rapidly evolving broad class of low-dimensional carbon-based nanomaterials, commonly defined as zero-dimensional nanostructures with characteristic dimensions below 10 nm and intrinsic photoluminescence arising from quantum confinement, surface states, and molecular-like emissive centres[1–3]. This class includes a range of structurally related systems, such as amorphous[4] and graphitic[5,6] carbon cores, with diverse surface functionalisation, which enables broad tunability of their optical response. Owing to their size-dependent emissions, excitation versatility, and compatibility with solution-based and thin-film fabrication techniques, CDs have been applied in photonics,[7,8] optoelectronics,[9,10] biochemical sensing,[11,12] light-emitting structures,[13,14] and functional optical coatings[15–17]. Compared to conventional luminescent nanomaterials such as semiconductor quantum dots and organic dyes, carbon dots offer advantages including enhanced photostability, lower toxicity, and scalable synthesis, while maintaining sufficient flexibility for integration into nanophotonic structures.[18,19] The steady increase in research activity in this field over the past decade has underscored the growing recognition of CDs as a promising alternative low-dimensional material platform that is particularly relevant to actively controlled photonic systems and metasurface-based optical devices.[20–22]

The absence of heavy metals in most CD systems generally translates into reduced toxicity and improved environmental compatibility,[23] whereas their chemically robust carbon framework ensures high resistance to photobleaching and chemical degradation[24]. Equally important is the inherently rich and accessible surface chemistry of CDs, which enables efficient functionalisation,[25] good processability, seamless incorporation into composite materials, and thin-film formation.[26–29] However, the structural and electronic characteristics that underlie these advantages impose fundamental limitations.[30] In particular, the prominent role of surface-related emissive states often results in a lower photoluminescence quantum yield compared to optimised

semiconductor quantum dots[31,32] as well as increased variability and limited reproducibility of optical properties.[33] Besides the difficulty of spectral control, CD photoluminescence often degrades significantly upon drying, limiting its performance in thin-film structures.[34]

The rapid development of carbon dots has been accompanied by the establishment of a wide range of synthesis strategies.[15] Commonly employed approaches include hydrothermal[35] and solvothermal methods,[36] microwave-assisted synthesis,[37,38] pyrolysis of organic precursors,[39] and electrochemical[40] and laser-based techniques.[41] The selection of a synthesis protocol directly influences the structural and chemical characteristics of the resulting CDs, and consequently, their suitability for specific functions.[15] Solution-based routes, particularly those performed in aqueous solutions, are the most widely used because of their manufacturability, accessibility, and high reproducibility.[42,43] These methods are often compatible with the principles of green chemistry,[44] enabling the use of harmless precursors under mild processing conditions. Consequently, most reported studies have focused on carbon dots dispersed in liquid media, where their optical properties can be readily characterised and optimised. In contrast, the solid-state configurations and thin films of CDs remain comparatively underexplored, despite their critical importance for photonic and metasurface-based applications.

The performance of CDs degrades significantly when they are transferred to dry form[45]. Upon solvent removal, the CDs tended to aggregate, leading to pronounced photoluminescence quenching[46,47] and a drastic reduction in the quantum yield.[48,49] In addition, the uncontrolled spatial distribution on substrates and poor coupling to optical modes further limit light extraction and light–matter interactions.[50] As a result, carbon dots exhibit substantially reduced optical efficiency, which hinders their direct implementation in photonic devices. A viable strategy to overcome these limitations is the formation of hybrid “carbon dots–substrate” structures, in which the substrate plays

an active optical role beyond mere mechanical support. In such systems, the surface morphology influences the spatial distribution of the CDs, whereas the optical properties of the substrate define the local electromagnetic field distribution. Morphologically structured substrates can increase the effective contact area, enhance the near-field optical confinement, and modify the excitation and emission processes of carbon dots, thereby providing a pathway toward improved and controllable solid-state performance.[34,51,52]

Nanowire (NW) platforms represent a highly promising class of substrates because of their high aspect ratios and large specific surface areas, which provide a high density of surface sites for emitter adsorption.[53,54] NWs can act as efficient waveguides, enabling light coupling, optical confinement, and enhanced interactions with luminescent centres.[55,56] These properties make these substrates particularly attractive for amplifying weakly emissive materials such as CDs. The substrate material itself is equally critical; it affects the surface chemistry, adhesion, and spatial distribution of the CDs, while the NW optical modes influence the photoluminescent response of the hybrid system.

In this study, we systematically investigated a hybrid approach employing the integration of CDs with NWs to achieve predictable solid-state CD emissions. We fabricated and characterised three distinct semiconductor NW platforms, GaN, GaP, and Si, as CD hosts. By combining numerical simulations with detailed photoluminescence spectroscopy, we explored the manner in which the electronic and optical properties of the host NWs governed the excitation and emission characteristics of the integrated CDs. Our work establishes general design principles for tailoring the fluorescence in these hybrid systems and evaluates their potential as manufacturable components for advanced photonic integration.

## Results and Discussion

### Materials synthesis and study

All the NWs in this study were synthesised on Si substrates, leveraging the cost-effectiveness and scalability of Si-based processes for future photonic integration. Direct synthesis of high-quality III-Vs on Si is challenging for planar films, where significant lattice and thermal expansion mismatches typically lead to high dislocation densities and film cracking. The NW architecture effectively circumvents these issues. Its large surface-to-volume ratio and nanoscale footprint allow for efficient strain relaxation at the lateral facets, resulting in crystals with exceptional structural perfection.[57] This inherent advantage of the NW morphology provides an ideal defect-scarce substrate for subsequent CDs deposition.

Among these, vertically aligned GaN NWs grown using plasma-assisted molecular beam epitaxy (PA-MBE) via a self-induced mechanism on (111)-oriented Si[58] have emerged as promising hosts for CD integration (Fig. 1a). GaN was selected because of its outstanding optoelectronic properties. With a wide direct bandgap of ~3.4 eV, GaN is highly transparent across the visible spectrum. This transparency is expected to prevent parasitic absorption of the photoluminescence (PL) of the CDs, thereby ensuring efficient light extraction. Furthermore, this property opens a pathway for engineering dual-colour emissions, where GaN NWs could potentially serve as intrinsic UV emitters alongside the visible emission of CDs. The refractive index of the material of ~2.3–2.4 in the visible range provides a favourable optical contrast with ambient media, enabling efficient waveguiding and directional propagation of light along the NW axis while mitigating excessive losses. This study builds on the well-established importance of nitride semiconductors in photonics. GaN and its ternary InGaN alloys form the backbone of modern visible and UV optoelectronics, with tuneable emissions from UV to infrared[59]. Thus, integrating CDs with GaN NWs introduces a new degree of freedom for luminescence control in this mature and

versatile material. Complementing these optical characteristics, the high thermal stability, mechanical robustness, and chemical inertness of GaN ensure the durability of the hybrid platform under operational conditions.

The GaN NWs utilised here, characterised by scanning electron microscopy (SEM), exhibited a high degree of morphological uniformity, with a length of approximately 2 μm and a well-defined hexagonal cross-section of ~300 nm (Fig. 1d). This structural regularity is paramount for achieving a consistent and reproducible photonic performance across the hybrid platform.

In parallel, we investigated gallium phosphide (GaP) NWs were investigated as complementary platforms for CDs integration. These NWs were synthesised directly on a (111)-oriented Si wafer via a self-catalysed vapour–liquid–solid (VLS) growth mechanism using molecular beam epitaxy (MBE)[34] (Fig. 1b). GaP NWs are well suited for photonic applications because their indirect wide bandgap (~2.26 eV) confers low optical absorption across the visible and near-infrared spectral ranges. This inherent transparency makes GaP NW an exceptional optical waveguide, as confirmed by our previous work demonstrating resonant optical phenomena and highly directional guidance of light within individual NWs.[57,60] The waveguiding effect is a critical asset for hybrid CD-NW systems. This can lead to a significant enhancement of the local optical pumping field for CDs deposited on the NW surface. This enhancement arose from the localisation of the electromagnetic field in the near-surface region of the NW and the precise location of the CDs, thereby potentially increasing their absorption and emission efficiencies.

In addition to passive waveguiding, GaP offers a versatile approach for advanced photonic engineering. Our group has previously shown that complex heterostructured GaP(As)-based NWs can be synthesised by introducing direct-bandgap alloys that emit light in the visible range.[61] Furthermore, GaP NWs have proven to be excellent hosts for hybrid integration with other promising luminescent materials, such as transition

metal dichalcogenides (TMDs), which serve as efficient nanoscale waveguides for emission.[55] This success positions GaP NWs as a robust and flexible platform for coupling with CDs. Additional favourable properties, such as a high refractive index (~3.2 at 600 nm) for strong light confinement and excellent chemical stability, further confirmed their suitability. GaP NWs used in this work, shown in Fig. 1e, are characterised by their high aspect ratio, with a length of approximately 25 μm and a uniform hexagonal cross-section with a diameter of about 300 nm. This considerable length is advantageous for studying extended waveguiding and the interaction between the propagating modes and integrated CD emitters.

Finally, we consider Si NWs, a platform whose significance is rooted in their foundational roles in modern technology. The synthesis of Si NWs is inherently compatible with the vast infrastructure of complementary metal-oxide-semiconductor (CMOS) processes, offering a direct and scalable pathway for integrating active photonic components with electronic circuitry on a single chip. This unparalleled fabrication advantage is critical for the development of commercially viable photonic platforms.

Although bulk Si is an indirect bandgap semiconductor and a poor emitter of light, its properties in NW geometry are transformative for photonics. The high refractive index (~3.5 at 600 nm) of Si provides strong optical confinement, enabling efficient waveguiding and the formation of high-quality optical resonances. Furthermore, the nanoscale morphology can lead to the relaxation of the selection rules and enhanced light-matter interactions, making Si NWs excellent passive photonic building blocks. Recent advancements have firmly established Si NWs as a leading platform for integrated nanophotonics, demonstrating functionalities such as low-loss waveguiding in the IR, optical filtering, and sensing.[54,62,63] Their primary utility lies in their ability to manipulate and guide light at the subwavelength scale, whereas absorption in the visible and near-infrared ranges is expected to suppress emission of the CDs.

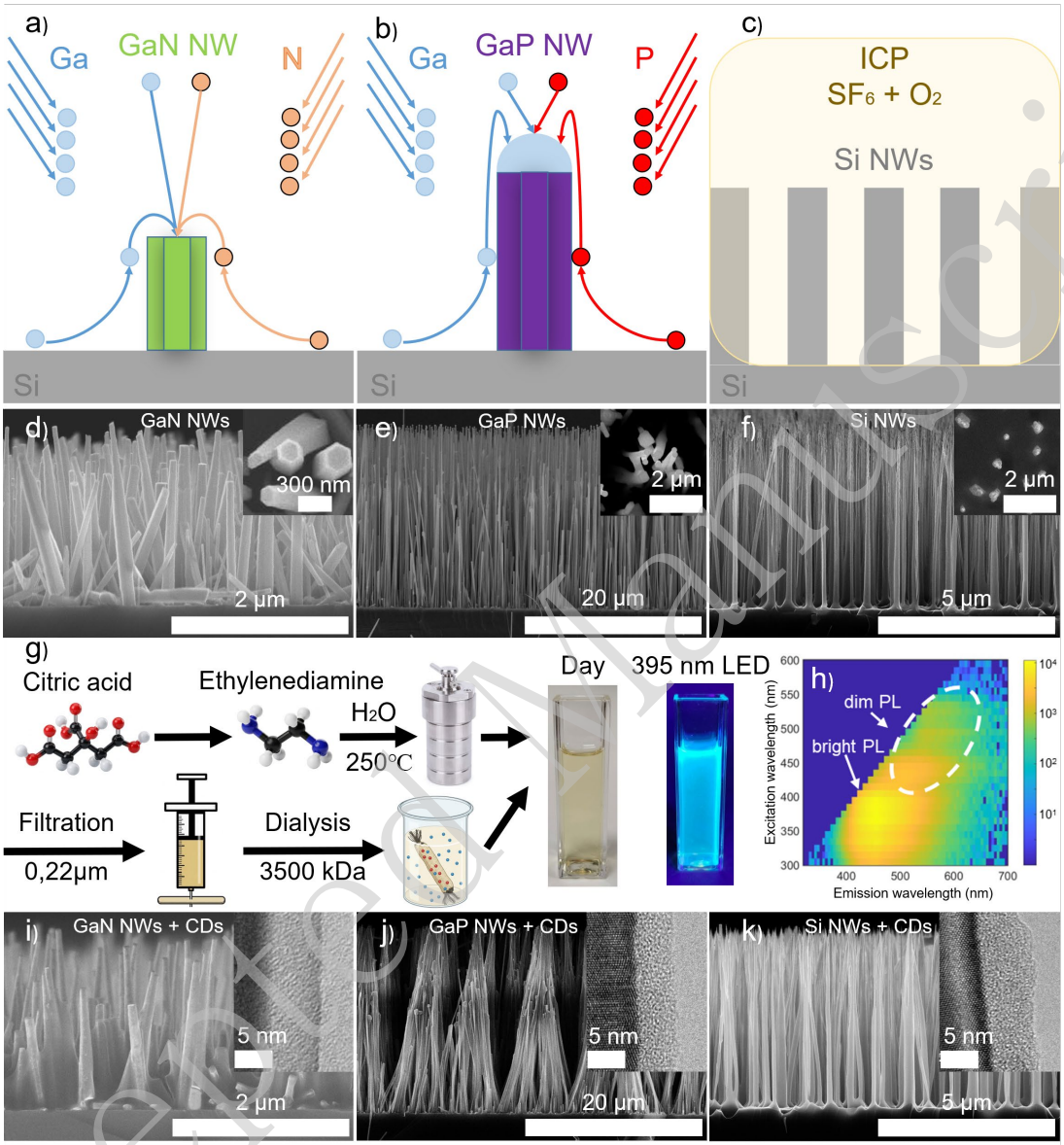


**Figure 1. Nanowires under study: a)** Schematic of GaN NWs synthesis by MBE via the self-induced growth mechanism. **b)** Schematic of GaP NWs synthesis by MBE via the self-catalysed vapor-liquid-solid growth mechanism. **c)** Schematic of Si NWs synthesis by plasma-chemical etching of a monocrystalline Si wafer. In-plane SEM images of as-grown **d)** GaN, **e)** GaP and **f)** Si NWs arrays with plane view images on insets. **g)** Step-by-step CDs' synthesis process and photos of the cuvette with CDs aqueous solution under daylight and UV LED flashlight (395 nm, 3 W). **h)** PL map of the CDs aqueous solution as a function of excitation wavelength (log scale). In-plane SEM images of **i)** GaN, **j)** GaP and **k)** Si NWs arrays decorated with CDs, insets demonstrate corresponding TEM images of the near-surface region of the structures.

The arrows in the schematics denote the molecular fluxes of the growth species during the MBE growth process, as well as the subsequent adatom surface diffusion along the NW sidewalls toward the growth interface.

The "cap" shown on top of the GaP NWs in Fig. 1b represents the liquid gallium (Ga) catalyst droplet, which drives the classical VLS growth mechanism. In contrast, the GaN NWs shown in Fig. 1a are grown via a self-induced (catalyst-free) mechanism, which is why they do not possess a metallic droplet at their tips.

Colours are used to distinguish between different materials and structural regions. For instance, specific colours distinguish the Si substrate from the grown III-V semiconductor materials (GaN and GaP), whereas in Fig. 1c, colour contrast is used to highlight the etched Si regions formed during the top-down inductively coupled plasma (ICP) process.

This approach bypasses the inherent emission limitations of Si and paves the way toward monolithically integrated light sources and complex photonic networks. The Si NWs utilised in this study were fabricated via the plasma-chemical etching of a boron (B)-doped monocrystalline (100) Si wafer (Fig. 1c) resulting in structures with high crystalline perfection required for consistent optical performance. The NWs have a length of approximately 10 μm and a cylindrical cross-section with a characteristic size of 300-350 nm (Fig. 1f).

CDs exhibiting blue luminescence under near-UV irradiation were synthesised using a common hydrothermal method[34,64] ( Fig. 1g). Information on the PL properties of the CDs in aqueous solution is presented as an excitation-emission map in Fig. 1h. The map clearly shows the most efficient emission upon 320-400 nm excitation. The CDs exhibited bright blue emission with a peak near 450 nm under this excitation. The emission intensity decayed by an order of magnitude with an increase in the excitation wavelength, providing dim emission peaks at 550 nm under 470 nm excitation and further red-shifting to 600 nm under 550 nm excitation. Thus, we conclude that the CDs

synthesised in aqueous solution exhibit bright blue luminescence upon UV excitation which shifts and gets dimmed toward green under blue excitation and further shifts to orange under green excitation.

The decoration of the NWs with CDs was carried out by drop-casting the CDs aqueous solution onto the surfaces of the GaN, GaP, and Si NWs. Because the difference in the specific surface area between the samples is governed by the difference in the NWs morphology, a CDs solution with the same concentration was used for all the samples, while its volume varied sample to sample, being proportional to the surface area of the NWs per unit area of the substrate (more details in Methods). This approach is expected to provide a uniform deposition of the CDs layer on the surfaces of NWs with different geometries. The results of this deposition are presented in Fig. 1i–k for GaN, GaP, and Si NWs. In the images obtained by transmission electron microscopy (TEM, Jeol JEM-2100, JEOL Ltd., Japan) from the near-surface region of the NWs decorated with dots, a layer of amorphous carbon coating with a thickness of approximately 5 nm was clearly visible and identical for all the samples. This layer cannot be associated with the NW material and is attributed to a layer of CDs with a thickness of 1-2 dots ( Fig. S4-S5 in Supplementary Information).[34,65] The consistent CDs layer thickness observed across different NW platforms validates the applicability of the proposed volume-correcting approach. However, the deposition process also induced a morphological change in the NW arrays, leading to bundling of the NWs at their tops. This effect was most pronounced for the longest GaP NWs (Fig. 1j), likely due to capillary forces during solvent evaporation and their high mechanical flexibility.[34]

**Numerical simulations**

Nanostructured surfaces, including metasurfaces, are complex in terms of their optical performances. For samples with semiconductor NWs, the optical phenomena can be additionally affected by their quasi-waveguiding behaviour rather than by simple

light scattering. Moreover, the NWs were non-uniform in length. To consider the influence of the NW material and dimensions on the emission spectrum of CDs placed over the NWs surface, we performed finite-difference time-domain (FDTD) modelling (see details in the Methods section). The resulting spectra, shown in Fig. 2b, e, h, demonstrate the signal scattered in the vertical upward direction by GaN, GaP, and Si NWs of different lengths. Although the simulated dipole sources initially emitted light with a uniform unity intensity across the entire wavelength range (380-800 nm), the recorded signal was generally 10 times lower and had pronounced spectral features. For example, NWs made of all three materials demonstrate broad spectral peaks in the 400-600 nm range for the smallest length NWs 0.14-1 μm. This can be explained by the fact that short NWs (with dimensions less than or approximately equal to the incident wavelengths) act as compact Mie scatterers, with a plethora of multipoles excited simultaneously.

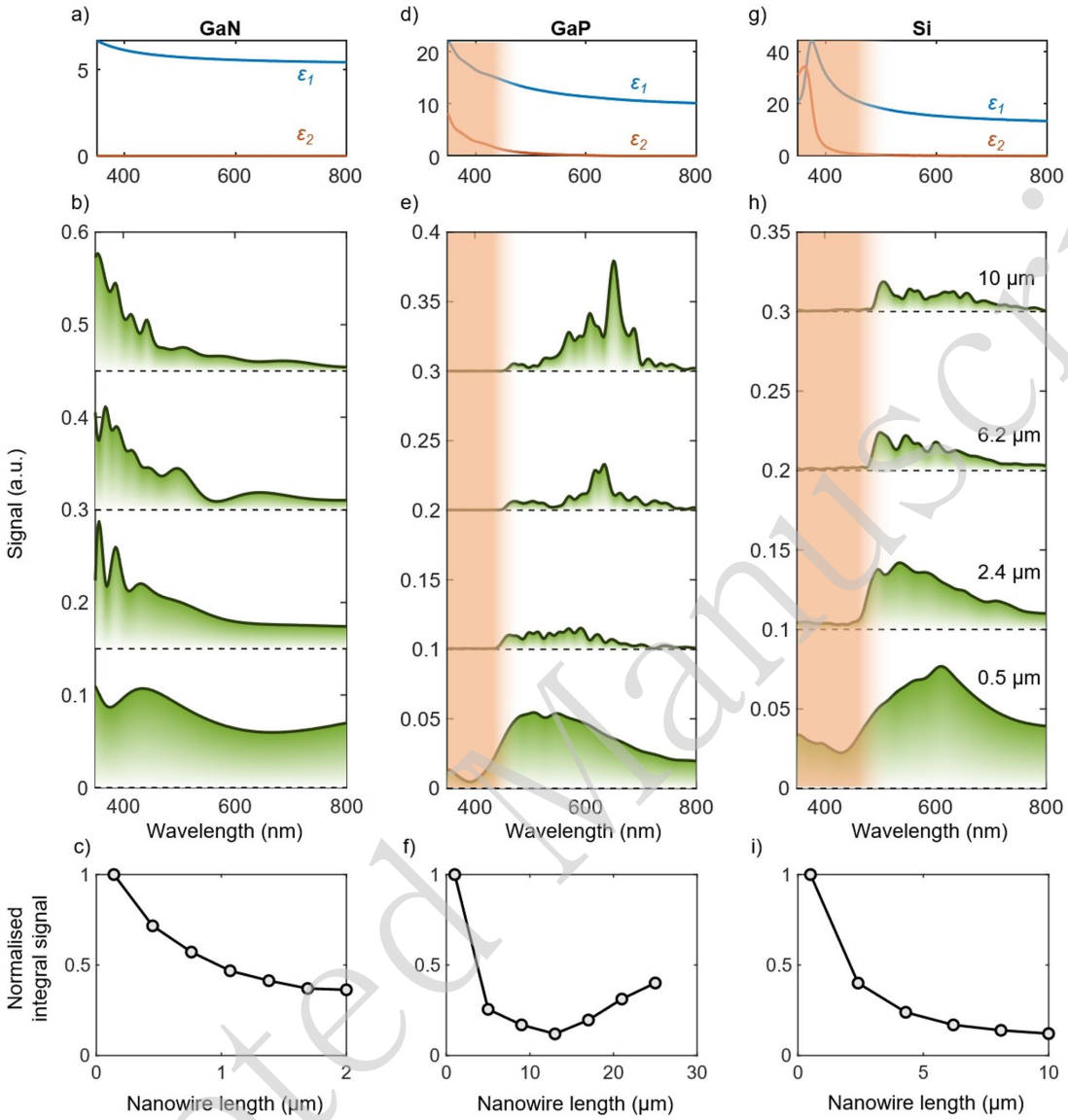


**Figure 2. PL simulation of CDs distributed along the NWs.** Dielectric partitivities of **a)**, GaN **d)** GaP and **g)** Si. Simulated spectra of light, emitted by point dipoles placed along the NWs and scattered by the NWs in the up direction: **b)** GaN, **e)** GaP and **h)** Si. These spectra are averaged over the dipole position along the NW and dipole orientations, see Methods section for details. Integral scattered signal over the whole visible spectrum for a series of NW lengths, normalised on unity **c)** GaN, **f)** GaP and **i)** Si.

The total response of the series of multipoles resulted in broad spectral features[66]. The spectral response changed dramatically as the NW length increased. For all three materials, the appearance of higher-frequency oscillations and redistribution of the

maximum signal between several peaks were observed. We attribute this to the collective effect of the Fabry–Pérot (due to light reflections between the NW faces), Mie, and waveguide modes. The latter modes appear in the NW as the core and air as the cladding. A further increase in the NW length, up to dozens of microns, should strengthen the contribution of the waveguide modes to the total emission. This was observed for long GaP NWs. It can be seen that the integral signal over the entire visible spectrum for GaP NWs (Fig. 2c) initially decreases as the NW length increases, similar to NWs made of other materials, such as GaN and Si (Fig. 2f,i). This can be explained by the increase in the total scattering efficiency of the semidielectric NWs with increasing volume. However, starting from ~13 μm length, the signal starts to grow again. This is an effect of the waveguide modes: the light emitted by the dipoles in the vicinity of the NW surface couples to the propagating modes and is efficiently transferred to the upper face of the NWs. This mechanism should be sensitive to material loss. For the two materials under study, the optical absorption of GaP and Si is significant in the short-wavelength region, which is denoted by the red gradient strips in Fig. 2d, g. One can see that in this highly absorptive region, the scattered signal was sufficiently suppressed, as shown in Fig. 2e, h.

An analysis of the data in Fig. 2 suggests that the intrinsic optical properties of the NW substrates significantly affect the properties of the fluorescent coatings. The use of GaN favours quantum dot PL in the blue-green region of the spectrum, whereas Si and GaP NWs retain only the long-wavelength tail of the overall PL signal owing to the intrinsic optical absorption of the material.

**CDs confocal fluorescence microscopy**

To visualise luminescence, the fabricated samples were analysed using confocal fluorescence microscopy. Fig. 3a–c depicts 3D fluorescence images of the samples demonstrating luminescence over the entire surface of all the NWs. For the experiment, a 488 nm wavelength laser and a 600–660 nm bandpass filter were used to detect the

response. The image acquisition conditions were identical for all three samples. It should be noted that luminescence was not observed in the bare NWs in the absence of CDs on the surface when using a 488 nm wavelength laser was used. The corresponding photon energy is insufficient to cause PL in GaN NWs, whereas GaP and Si NWs do not exhibit PL owing to their indirect bandgap structures.

To analyse the emission efficiency, we calculated the emission intensity of the samples by considering the sum of the pixel luminescence intensities from all the image layers. Considering the specific surface area of the NWs, the emission intensity per unit surface area of a single NW was determined. The results were $2.3 \cdot 10^6$, $7.0 \cdot 10^6$ and $0.3 \cdot 10^6$ arbitrary units for GaN, GaP, and Si NWs, respectively (Fig. 3d).

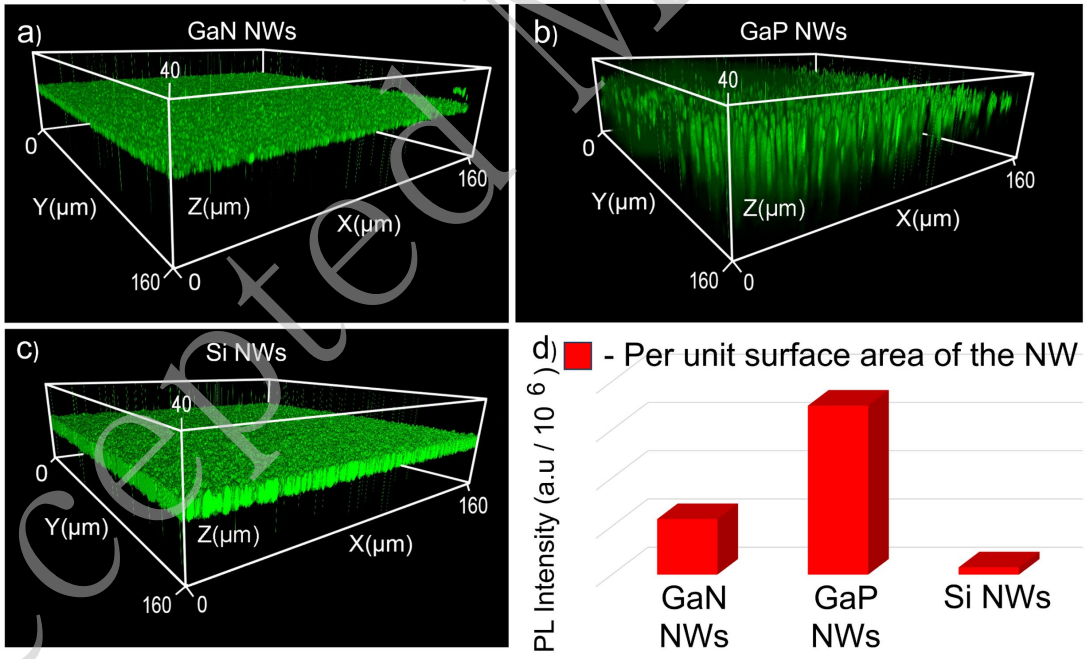


**Figure 3. NW/CDs structures confocal fluorescence microscopy.** Images of the decorated **a)** GaN, **b)** GaP, and **c)** Si NWs. **d)** Histogram of the emission intensity per unit surface area of the samples.

Thus, the data in Fig. 1i-k and Fig. 3a-c collectively allow us to conclude the

presence of a uniform layer of CDs on the surface of the NWs, exhibiting PL in the orange-red range. GaP exhibits the highest emission intensity per unit surface area for a single NW. This phenomenon is discussed in detail below:

**Photoluminescence spectroscopy**

To obtain more details on the PL of the NW/CD structures, we obtained the excitation-emission 2D maps presented in Fig. 4a–c. Fig. 4a shows a false-colour excitation-emission map for GaN NWs/CDs on a log scale to enhance the visibility of the major PL bands. The two most prominent ones are clearly visible on inset in Fig. 4a plotted in linear scale. These include deep level emission (DLE) in GaN NWs with a peak at 580 nm (denoted in Fig. 4a as "DLE") at excitations 350-375 nm. The second is the dim CDs emission band peaked near 550 nm under 430 nm excitation (denoted in Fig. 4a as "CDs' dim PL"). The occurrence of the DLE band and its origin were studied by investigating the bare GaN NWs excitation-emission map presented in the Supporting Information and demonstrating the presence of this particular band (see Fig. S1). This emission, which is known to arise from nitrogen vacancy centres, has been well documented in prior studies.[67]

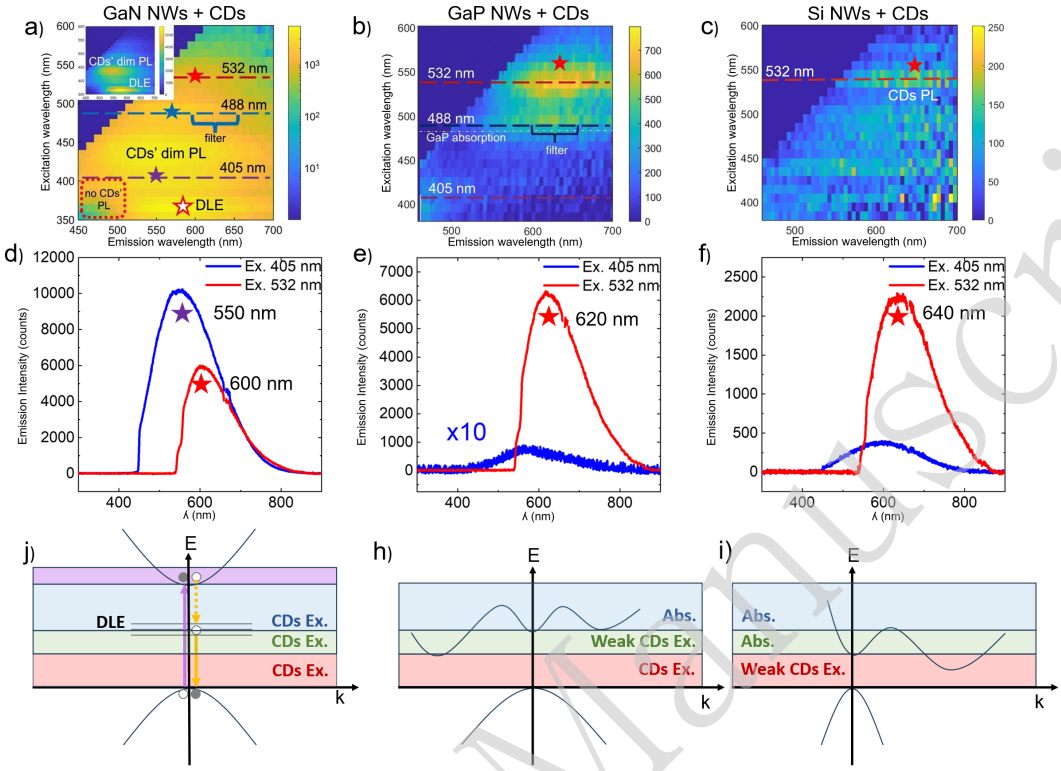


**Figure 4. NW/CDs structures PL spectroscopy.** Excitation-emission maps of **a)** GaN, **b)** GaP, and **c)** Si NW/CDs structures. PL spectra of **d)** GaN, **e)** GaP, and **f)** Si NW/CDs structures under 405 nm and 532 nm laser excitation. Band diagrams of **j)** GaN, **h)** GaP, and **i)** Si allowing for the visualisation of processes occurring during the excitation of CDs' PL on the NW surfaces.

The dim PL observed is attributed to the CDs with a slight red shift relative to the emission of CDs in aqueous solution (Fig. 1h). This red shift is not associated with the properties of the GaN NWs but rather corresponds to the previously discussed conformational changes in the surface functional groups, leading to variations in their PL spectra.

Additionally, all the samples were investigated by PL spectroscopy under laser excitation at wavelengths of 405 and 532 nm (Fig. 4d-f). The PL spectra of the GaN NWs with CDs under both excitations depicted in Fig. 4d are in a good agreement with the map in Fig. 4a. The measurements demonstrate that the structure exhibits PL peak

of CDs near 550 nm under 405 nm excitation which decays and red-shifts toward 600 nm under 532 nm excitation.

One of the most important observations with GaN NWs was the absence of blue PL CDs under UV excitation. Despite the presence of dim PL CDs under visible light excitation which is comparable in intensity to DLE, the expected bright PL peak near 450 nm was not observed. This is expected to be the result of the strong absorption of excitation in the GaN NWs which in turn results in an intense DLE. Fig. 4j depicts the GaN band diagram with highlighted ranges of excitation photon energies (the colour corresponds to the excitation), allowing interpretation of the spectroscopy data. Upon UV excitation near the absorption edge, we observed the recombination of deep-level defects in GaN. All absorption occurred in GaN; therefore, no PL corresponding to the CDs was observed. A reduction in the excitation energy below the GaN bandgap leads to excitation of the PL of the CDs, which red-shifts with an increase in the excitation wavelength.

Next, we discuss the PL of GaP NWs decorated with CDs. Fig. 4b depicts a linear-scale PL map of the sample exhibiting two major PL bands, both peaking near 620 nm: a more intense band under 532 nm and a dim band upon 488 nm excitation. These emissions correspond to the PL red shift compared with the GaN NWs. Surprisingly, no PL was observed upon excitation at wavelengths below 480 nm. This result is in perfect agreement with the PL spectra measured under 405 nm and 532 nm laser excitations, as plotted in Fig. 4e. Compared with GaN NWs, GaP NWs exhibit neither bright blue PL upon UV excitation nor dim PL below 500 nm. The latter value corresponded to the absorption edge of GaP. Thus, we confirmed that PL was not excited in the CDs below the absorption edge of the host material. The schematic of the GaP band structure in Fig. 4h shows that absorption in GaP restricts the PL excitation of CDs to the green-orange-red visible range.

Despite the calculated emission intensity per unit surface area from confocal

microscopy data suggesting a threefold higher PL efficiency for CDs on GaP NWs, the excitation-emission maps in Fig. 4a and 4b indicate an overall higher PL intensity for the GaN-based hybrid platform. This apparent contradiction can be reconciled by considering the specific spectral conditions of different measurements. Confocal intensity values were acquired under 488 nm excitation and detected within a 600-660 nm filter window. The corresponding cross-sections on the maps in Fig. 4a a and 4b reveal that the majority of the emission of CDs on GaN NWs lies below 600 nm, meaning that they were largely filtered out during the confocal measurement. In contrast, the most intense PL from CDs on GaP NWs was spectrally positioned within the 600-660 nm detection range, leading to preferential measurement. Furthermore, potential variations in the excitation efficiency due to sample positioning and size in broadband PL measurements introduce additional uncertainty.

Finally, we studied the Si NWs decorated with CDs. Fig. 4c depicts the PL map of the sample, showing noisy low-intensity values with a very dim band that peaked near 640 nm under 532 nm excitation. This was confirmed by PL spectroscopy under 532 nm excitation (see Fig. 4f) and corresponds to the PL of the CDs. Despite the noisy map in Fig. 4c without intense emission bands, excitation with a 405 nm laser deep inside the Si absorption band led to the measurable PL of the CDs, as shown in Fig. 4f. Again, we associated the low PL intensity throughout the entire measurement range with the absorption in the host material, Si. A schematic of the Si band structure is shown in Fig. 4i.

## Conclusion

In summary, this study demonstrates a versatile and manufacturable strategy for creating nanostructured fluorescent emitters by hybridising solution-processed CDs with single-crystalline semiconductor NWs. We systematically investigated how the electronic properties of the host material dictate the photophysical response of the integrated CDs. A critical general finding is that the absorption edge of NW acts as a

definitive spectral filter; efficient excitation of PL of CDs occurs only for photon energies below this edge, whereas higher-energy photons are absorbed parasitically by the host. This principle was elucidated across three distinct platforms: GaN NWs allow the broadest excitation window in the visible range, GaP NWs provide high-efficiency PL limited to the green-red spectrum, and Si NWs highlight the tradeoff between CMOS compatibility and visible-range absorption losses.

The synthesis leveraged scalable bottom-up (GaN and GaP) and top-down (Si) NW fabrication on Si substrates, ensuring a pathway for integration. Beyond spectral filtering, the NW morphology actively enhances performance through optical confinement and waveguiding, which is particularly evident in GaP structures. This study establishes a clear framework for rationally selecting host NW based on the target emission window and application. By combining the tuneable luminescence of CDs with tailored optoelectronic properties and scalable processing of semiconductor NWs, this approach offers a powerful and flexible platform for the development of integrated nanophotonic light sources for sensing, on-chip communication, and quantum technologies.

## Materials and Methods

### Numerical simulations

To understand how the NW-based morphology affects the emission signal from the deposited quantum dots, FDTD-based numerical simulations were performed. The unit cell contains a single vertically aligned NW. Although the experimental data show considerable deviations in the NW orientations from the vertical alignment, the model considers only vertically positioned NWs, as this is a critical geometric feature. The NW base diameter was set according to the SEM images shown in Fig. 1. The signal $I_d(\lambda,h,H,\theta,\varphi)$ is emitted by a dipole at a certain wavelength $\lambda$, at position h along the NW (the dipole's distance from the surface), and dipole orientation ($\theta,\varphi$) along the x,

y, or z axes. The carbon layer on the surface of the NWs is very thin (5 nm) and provides optical contrast between the employed semiconductor materials and carbon structures, and therefore does not introduce any noticeable perturbations in light propagation considering the large dimensions of the NWs and visible wavelengths considered. Moreover, CDs with estimated sizes 2.5 nm – 5 nm physically act uniquely as light emitters[68] (single dipole sources) without any optical resonant properties[69,70]. GaP and GaN NWs were considered hexagonal and Si NWs cylindrical according to the morphology of the samples obtained via SEM (see Fig. 1). For every dipole arrangement, the intensity $I_{scat}(\lambda,h,H,\theta,\varphi)$ of the optical signal propagated through the NW and scattered upwards is recorded by a horizontally oriented field monitor placed 100 nm above the NW. To obtain the final structure-modified optical signal $I_{final}$, propagated through the NWs and emitted from dipoles in different arrangements, we performed the following averaging procedure:

$$I_{final}(\lambda, N_H) = \frac{1}{3N_h}\sum_{\theta,\varphi}\sum_{h}\sum_{H}\frac{I_{scat}(\lambda, \mathrm{h}, \mathrm{H}, \theta, \varphi)}{I_d(\lambda, \mathrm{h}, \mathrm{H}, \theta, \varphi)}, \quad (1)$$

where the averaging was performed over three mutually perpendicular dipole orientations and $N_h$ dipole positions along the NW ($N_h = 5$). Several NW lengths ($NH$ = *6–7*) were considered for each material, up to the longest experimentally observed lengths.

**Growth of GaN NWs**

The growth experiments were performed on single-side-polished n-type Si substrates using a Riber Compact 12 MBE system. The substrate surface orientation was (111) with a 4° miscut toward the [110] direction. First, the substrate was loaded into an MBE chamber and thermally annealed at 950 °C (according to thermocouple measurements) for 20 min. Annealing of the Si substrate prior to growth was performed directly in the MBE growth chamber. The residual pressure in the chamber

was ~$5\cdot10^{-11}$ Torr before annealing and ~$3\cdot10^{-9}$ Torr and after annealing. The substrate temperature was then decreased to 600 °C, and the nitrogen plasma was ignited to form a $Si_xN_y$ thin layer. A $Si_xN_y$ layer was introduced to increase the diffusion length of the Ga adatoms and suppress parasitic GaN nucleation on the $Si_xN_y$ surface. In combination with preformed GaN nuclei, this approach enables relatively low-density nanowire growth; GaN growth is suppressed on the $Si_xN_y$ surface between the nuclei, while the nuclei act as preferential sites for subsequent GaN nanowire formation[71]. The plasma source was operated at a power of 450 W and a nitrogen flow rate of 0.4 sccm for 30 min. The working pressure during the growth was maintained at $7.4\cdot10^{-6}$ Torr. Next, Ga was deposited onto the formed $Si_xN_y$ layer for 15 s in the absence of nitrogen plasma to form Ga droplets. Subsequently, the nitrogen plasma was ignited again under the same source parameters, and the surface with the Ga droplets was nitrided for 45 min. This procedure was used to form GaN nuclei that served as seeds for further GaN NW growth. Subsequently, the substrate temperature was increased to 820 °C, the Ga shutter was opened, and the growth of the GaN NWs continued for 16 h 25 min. The beam-equivalent pressure of Ga was maintained at $1.5\cdot10^{-7}$ Torr throughout all stages of the growth process. This approach allows the fabrication of relatively low-density GaN NWs compared with conventional self-induced GaN NWs on Si(111) substrates.

**Growth of GaP NWs**

The NW arrays were grown using a Veeco GEN-III solid-source MBE system equipped with a Ga effusion cell and a valved phosphorus-cracking cell. GaP NWs were formed via a self-catalytic VLS growth mechanism[72] on Shiraki-cleaned[73] $SiO_x$/Si(111) wafers with a silicon oxide layer prepared via wet chemical oxidation in an aqueous solution of ammonia and hydrogen peroxide ($NH_4OH$:$H_2O_2$:$H_2O$ with a volume ratio of 1:1:3).[74] Pre-growth annealing at 780 °C for 30 min facilitated the generation of defects in the oxide layer, promoting the self-assembly of GaP NWs

initiated by the simultaneous opening of the Ga and $P_2$ fluxes. A two-stage growth procedure was implemented to independently control the length and diameter of the NWs. Details of the two-step approach are presented in a previous report.[75] To achieve a high yield of vertical GaP NWs, the first growth step was carried out at a high $P_2$/Ga flux ratio of 30 and a substrate temperature of 630 °C for 33 min. In the second step, the growth was continued for 3 h at a lower V/III ratio and reduced growth temperature to obtain the desired length and diameter of the NWs. The transition to the second growth stage involved a smooth 3-fold increase in Ga flux from 3 nm/min (beam equivalent pressure of a Ga flux beam of $8 \times 10^{-8}$ Torr) up to 9 nm/min (beam equivalent pressure of a Ga flux beam of $2.4 \times 10^{-7}$ Torr) and a decrease in growth temperature from 630 °C to 615 °C over a period of 900 s. The growth step transition was carried out without interrupting the growth process, while maintaining a constant phosphorus flux.

**Etching of Si NWs**

An unpolished p-type Si (100) wafer with a resistivity of 12 Ω·cm was used. The native oxide layer was not removed prior to the etching. Cryogenic etching was performed using an Oxford Plasmalab System 100 ICP380 at a temperature of −150 °C. The $SF_6$ and $O_2$ gas flow rates were maintained at 50 and 11 sccm, respectively. The pressure was maintained at 5 mTorr and the ICP power was fixed at 1000 W. An RF power (13.56 MHz) of 30 W was applied, resulting in a DC bias of 190 V. The etching time was set to 440 s. This process resulted in a uniform array of Si wires with a height of 10 μm and diameters of 300–350 nm. These wires were formed without using a mask or lithography, solely through self-organisation during the cryogenic anisotropic etching process. The residual pressure in the chamber was $10^{-7}$ Torr.

**Synthesis and Study of CDs**

CDs were synthesised using a common hydrothermal method[64] (Fig. 1g). The

following precursors were added to the autoclave with a Teflon beaker: 1.05 g of citric acid (Sigma-Aldrich), 340 μL of ethylenediamine (Sigma-Aldrich), and 10 mL of distilled water. The solution was stirred until citric acid was completely dissolved. Then, the autoclave was placed in an oven for 5 h at 200 °C. After cooling, the reaction products were filtered through a syringe filter with a pore diameter of 0.22 μm to remove larger particles. The filtered solution was dialysed (MWCO 3.5 kDa) for 24 h to remove the low-molecular-weight compounds and unreacted residues. The photoluminescence properties of the CDs in aqueous solution were measured using a BioTek Synergy H4 Hybrid Multi-Mode Microplate Reader and are presented as an excitation-emission map in Fig. 1h.

**Decoration of NWs with CDs.**

The NWs were decorated with CDs by drop-casting an aqueous solution of CDs onto the surfaces of the GaN, Si, and GaP NWs. The volume of the aqueous solution was proportional to the specific surface area of the NWs per unit area of the Si substrate. The surface area of a single NW is calculated based on its geometric parameters. The lengths were 2 μm for GaN NWs, 8 μm for Si NWs, and 25 μm for GaP NWs. The characteristic diameters of the GaN, Si, and GaP were 300, 350, and 300 nm, respectively. Additionally, top-view SEM images were used to estimate the density of the NWs per unit area of the growth substrate. The estimation was performed using open-source software ImageJ (Wayne Rasband, USA). This yielded NW-to-substrate area ratios of 90 for GaN NWs, 5.5 for Si NWs, and 20 for GaN, Si, and GaP NWs, respectively. Consequently, a droplet of a specific volume was applied to each NW array. The samples were then exposed to the solution for 5 h until the CDs completely sedimented. This procedure ensured identical deposition conditions for all the NW surfaces. After 5 h, the remaining aqueous solvent was removed from the substrates using a nitrogen flow.

Although conventional approaches for forming conformal coatings on nanostructured surfaces often favour alternative methods,[76] we chose drop-casting for CD deposition from an aqueous solution. This approach effectively utilises capillary forces and ensures complete coating of the complex NW morphology. The liquid phase acted as a vehicle, delivering the fluorescent agent deep into the gaps between the NWs. This process resulted in a uniform luminescent coating throughout the entire height of the NW array, as clearly demonstrated by the 3D confocal photoluminescence maps (Fig. 3).

The hybrid structures fabricated using CDs from different synthesis batches exhibited the same optical behaviours and overall properties, indicating that the results reported in this study are reproducible and not dependent on a specific batch of CDs.

**Confocal microscopy**

Confocal microscopy was used to analyse the samples. This technique collects luminescence from a specific optical section approximately 300 nm thick. To visualise the 3D structure, volumetric images were constructed by sequentially capturing images at 300 nm intervals (a Z-stack) and digitally stitching them together. A 488 nm laser was used for excitation, and the emitted signal was collected using a 600–660 nm bandpass filter. Images were acquired and processed using AxioVision software (Carl Zeiss Microscopy, Germany). All imaging conditions were identical for all three samples. To obtain the integral emission of the samples (Fig. 3d), the pixel luminescence intensities from all layers were summed using the Gwyddion software (GNU General Public Licence, Czech Republic, open-source software package). We also obtained the length and diameter distributions of the NWs by SEM image analysis. From these distributions, we extracted the mean geometric parameters to calculate the average surface area of the NWs per unit substrate area. The measured intensity was normalised to the calculated average area.

**PL spectroscopy**

PL measurements were performed using a home-built optical setup based on ThorLab components. The setup was equipped with two continuous-wave diode laser sources (405 and 532 nm), a 10× objective (Mitutoyo M Plan Apo, NA = 0.28), and a fibre-coupled spectrometer (Optosky ATP5020P). The excitation power was set at 1 mW.

**Spectral fluorimetry**

A BioTek Synergy H4 Hybrid Multi-Mode Microplate Reader was used to measure the photoluminescent properties of CDs in aqueous solution and on the surfaces of all three types of NWs. Although this method was originally developed for liquid-dye analysis, it can be adapted for use with solid samples by adjusting the height of the PL signal collected above the surface.

**Acknowledgements**

V.M.K. acknowledges support from the Russian Science Foundation (grant No. 25-72-00140) for the synthesis of GaP NWs and study of their morphology and optical properties, and for the numerical modelling.

A.V.S. acknowledges support of the TEM studies by the Russian Science Foundation (Grant No. 25-12-00154). S.V.B. acknowledges support of spectral fluorimetry from the Ministry of Science and Higher Education (Agreement No. 075-03-2025-662, project FSMG-2025-0003). M.A.A. thanks the Ministry of Science and Higher Education of the Russian Federation (project FSMG-2025-0005) for support of optical spectroscopy. A.D.B. acknowledges Russian Science Foundation (Grant 24-12-00225) for support of samples preparation. A.S.G. acknowledges the support from the Ministry of Science and Higher Education of the Russian Federation (research project 0791-2026-0035) for the synthesis of Si NWs (Si fibres). E.P.K., K.P.K. and I.S.M. thank the Ministry of Science and Higher Education of the Russian Federation (Grant FSRM-2026-0004) for supporting the processing, SEM studies and manipulation of the NWs and CDs. V.O.G., T.Sh., and G.E.C. acknowledge Saint-Petersburg State

University for the GaN nanowire growth (research project 122040800254-4).

**Author Contributions**

A.D.B. and V.M.K. supervised the study. V.M.K. and A.D.B. conceived the experiments. V.M.K., A.A.U., E.P.K., I.A.K., and A.K. carried out the experiments. A.A.U. and V.M.K. developed the numerical simulation methods. All authors participated in the data analysis and contributed to the writing of the manuscript.

**Data availability**

The authors undertake to provide materials, data, code, and related protocols (if applicable) as soon as possible to readers upon their request without any reservations.

**Conflict of interest**

The authors declare no competing interests.

**Supplementary information**

Supplementary materials are available online. The supplementary materials contain the PL maps of GaN, GaP, and Si NWs before and after CD deposition (Fig. S1, S2, and S3, respectively). A high-resolution transmission electron microscopy (HRTEM) image of the bare CDs on a TEM grid is shown in Fig. S4. TEM images of the bare CDs and their size distributions are presented in Fig. S5.

## References

1 Sun, Y. P. et al. Quantum-sized carbon dots for bright and colorful photoluminescence. *Journal of the American Chemical Society* **128**, 7756-7757 (2006) doi: 10.1021/ja062677d.

2 Kang, Z. H. & Lee, S. T. Carbon dots: advances in nanocarbon applications. *Nanoscale* **11**, 19214-19224 (2019) doi: 10.1039/c9nr05647e.

3 Li, S. et al. The development of carbon dots: from the perspective of

materials chemistry. *Materials Today* **51**, 188-207 (2021) doi: 10.1016/j.mattod.2021.07.028.

4 Siddique, A. B. et al. Amorphous carbon dots and their remarkable ability to detect 2,4,6-trinitrophenol. *Scientific Reports* **8**, 9770 (2018) doi: 10.1038/s41598-018-28021-9.

5 Hola, K. et al. Photoluminescence effects of graphitic core size and surface functional groups in carbon dots: $COO^-$ induced red-shift emission. *Carbon* **70**, 279-286 (2014) doi: 10.1016/j.carbon.2014.01.008.

6 Barman, M. K. & Patra, A. Current status and prospects on chemical structure driven photoluminescence behaviour of carbon dots. *Journal of Photochemistry and Photobiology C: Photochemistry Reviews* **37**, 1-22 (2018) doi: 10.1016/j.jphotochemrev.2018.08.001.

7 Xie, A. Q. et al. Carbon dots promoted photonic crystal for optical information storage and sensing. *Chemical Engineering Journal* **415**, 128950 (2021) doi: 10.1016/j.cej.2021.128950.

8 Zhang, Y. Q. & Lu, S. Y. Lasing of carbon dots: chemical design, mechanisms, and bright future. *Chem* **10**, 134-171 (2024) doi: 10.1016/j.chempr.2023.09.020.

9 Li, X. M. et al. Carbon and graphene quantum dots for optoelectronic and energy devices: a review. *Advanced Functional Materials* **25**, 4929-4947 (2015) doi: 10.1002/adfm.201501250.

10 Choi, H. et al. Versatile surface plasmon resonance of carbon-dot-supported silver nanoparticles in polymer optoelectronic devices. *Nature Photonics* **7**, 732–738 (2013) doi: 10.1038/nphoton.2013.181.

11 Zhu, S. J. et al. Highly photoluminescent carbon dots for multicolor patterning, sensors, and bioimaging. *Angewandte Chemie* **125**, 4045-4049 (2013) doi: 10.1002/ange.201300519.

12 Zhang, J. & Yu, S. H. Carbon dots: large-scale synthesis, sensing and bioimaging. *Materials Today* **19**, 382-393 (2016) doi: 10.1016/j.mattod.2015.11.008.

13 Hola, K. et al. Carbon dots - emerging light emitters for bioimaging,

cancer therapy and optoelectronics. *Nano Today* **9**, 590-603 (2014) doi: 10.1016/j.nantod.2014.09.004.

14 Barhum, H. et al. In-brain multiphoton imaging of vaterite cargoes loaded with carbon dots. *Nano Letters* **24**, 8232-8239 (2024) doi: 10.1021/acs.nanolett.4c00325.

15 Liu, H. X. et al. A review of carbon dots in synthesis strategy. *Coordination Chemistry Reviews* **498**, 215468 (2024) doi: 10.1016/j.ccr.2023.215468.

16 Yu, H. J. et al. Smart utilization of carbon dots in semiconductor photocatalysis. *Advanced Materials* **28**, 9454-9477 (2016) doi: 10.1002/adma.201602581.

17 Wang, B. Y. & Lu, S. Y. The light of carbon dots: from mechanism to applications. *Matter* **5**, 110-149 (2022) doi: 10.1016/j.matt.2021.10.016.

18 Resch-Genger, U. et al. Quantum dots versus organic dyes as fluorescent labels. *Nature Methods* **5**, 763-775 (2008) doi: 10.1038/nmeth.1248.

19 Liu, Y. H. et al. Advances in carbon dots: from the perspective of traditional quantum dots. *Materials Chemistry Frontiers* **4**, 1586-1613 (2020) doi: 10.1039/d0qm00090f.

20 Romero, M. R. & Bracamonte, A. G. Optical active meta-surfaces, -substrates, and single quantum dots based on tuning organic composites with graphene. *Materials* **17**, 3242 (2024) doi: 10.3390/ma17133242.

21 Dai, C. J. et al. Switchable unidirectional emissions from hydrogel gratings with integrated carbon quantum dots. *Nature Communications* **15**, 845 (2024) doi: 10.1038/s41467-024-45284-1.

22 Döring, A., Ushakova, E. & Rogach, A. L. Chiral carbon dots: synthesis, optical properties, and emerging applications. *Light: Science & Applications* **11**, 75 (2022) doi: 10.1038/s41377-022-00764-1.

23 Peng, X. G. et al. Shape control of CdSe nanocrystals. *Nature* **404**, 59–61 (2000) doi: 10.1038/35003535.

24 Baker, S. N. & Baker, G. A. Luminescent carbon nanodots: emergent nanolights. *Angewandte Chemie International Edition* **49**, 6726-6744 (2010) doi: 10.1002/anie.200906623.

25 Yan, F. Y. et al. The fluorescence mechanism of carbon dots, and methods for tuning their emission color: a review. *Microchimica Acta* **186**, 583 (2019) doi: 10.1007/s00604-019-3688-y.

26 Wang, Z. J. et al. Carbon dots based nanocomposite thin film for highly efficient luminescent solar concentrators. *Organic Electronics* **62**, 284-289 (2018) doi: 10.1016/j.orgel.2018.08.020.

27 Zhang, Y. J. et al. Efficient and stable white fluorescent carbon dots and CD-based glass thin-films: *via* screen-printing technology for use in W-LEDs. *RSC Advances* **7**, 49542-49547 (2017) doi: 10.1039/c7ra09924j.

28 Kouloumpis, A. et al. Graphene/carbon dot hybrid thin films prepared by a modified Langmuir-Schaefer method. *ACS Omega* **2**, 2090-2099 (2017) doi: 10.1021/acsomega.7b00107.

29 Li, Y., Li, S. & Zhang, K. S. Influence of hydrophilic carbon dots on polyamide thin film nanocomposite reverse osmosis membranes. *Journal of Membrane Science* **537**, 42-53 (2017) doi: 10.1016/j.memsci.2017.05.026.

30 Han, Y. et al. Synthesis, optical properties and applications of red/near-infrared carbon dots. *Journal of Materials Chemistry C* **10**, 11827-11847 (2022) doi: 10.1039/d2tc02044k.

31 Mintz, K. J., Zhou, Y. Q. & Leblanc, R. M. Recent development of carbon quantum dots regarding their optical properties, photoluminescence mechanism, and core structure. *Nanoscale* **11**, 4634-4652 (2019) doi: 10.1039/c8nr10059d.

32 Liu, H. F. et al. Synthesis of luminescent carbon dots with ultrahigh quantum yield and inherent folate receptor-positive cancer cell targetability. *Scientific Reports* **8**, 1086 (2018) doi: 10.1038/s41598-018-19373-3.

33 Noun, F., Manioudakis, J. & Naccache, R. Toward uniform optical properties of carbon dots. *Particle & Particle Systems Characterization*

**37**, 2000119 (2020) doi: 10.1002/ppsc.202000119.

34 Zakharov, V. V. et al. Hybrid photonic structures: gallium phosphide nanowires decorated with carbon dots for enhanced broadband emission. *Advanced Optical Materials* **12**, 2303198 (2024) doi: 10.1002/adom.202303198.

35 Kapitonov, A. N. et al. Hydrothermal synthesis of carbon dots and their luminescence. *AIP Conference Proceedings* **2041**, 030003 (2018) doi: 10.1063/1.5079363.

36 Zhang, Y. et al. Solvothermal synthesis of functionalized carbon dots from amino acid as an eco-friendly corrosion inhibitor for copper in sulfuric acid solution. *Journal of Colloid and Interface Science* **604**, 1-14 (2021) doi: 10.1016/j.jcis.2021.07.034.

37 Wang, X. H. et al. Microwave assisted one-step green synthesis of cell-permeable multicolor photoluminescent carbon dots without surface passivation reagents. *Journal of Materials Chemistry* **21**, 2445-2450 (2011) doi: 10.1039/c0jm02963g.

38 De Medeiros, T. V. et al. Microwave-assisted synthesis of carbon dots and their applications. *Journal of Materials Chemistry C* **7**, 7175-7195 (2019) doi: 10.1039/c9tc01640f.

39 Ortega-Liebana, M. C. et al. Uniform luminescent carbon nanodots prepared by rapid pyrolysis of organic precursors confined within nanoporous templating structures. *Carbon* **117**, 437-446 (2017) doi: 10.1016/j.carbon.2017.03.017.

40 Yu, T. Q. et al. Exploiting carbon quantum dots synthesized by electrochemical exfoliation for flexible resistance switching. *ACS Materials Letters* **6**, 793-800 (2024) doi: 10.1021/acsmaterialslett.3c01258.

41 Cortes, F. R. U. et al. A review on pulsed laser-based synthesis of carbon and graphene quantum dots in liquids: from fundamentals, chemistry to bio applications and beyond. *The Journal of Physical Chemistry C* **129**, 10378-10414 (2025) doi: 10.1021/acs.jpcc.5c01343.

42 Hu, Y. P. et al. Ethanol in aqueous hydrogen peroxide solution:

hydrothermal synthesis of highly photoluminescent carbon dots as multifunctional nanosensors. *Carbon* **93**, 999-1007 (2015) doi: 10.1016/j.carbon.2015.06.018.

43 Wang, C. X. et al. A hydrothermal route to water-stable luminescent carbon dots as nanosensors for pH and temperature. *Carbon* **82**, 87-95 (2015) doi: 10.1016/j.carbon.2014.10.035.

44 Sharma, V. Tiwari, P. & Mobin, S. M. Sustainable carbon-dots: recent advances in green carbon dots for sensing and bioimaging. *Journal of Materials Chemistry B* **5**, 8904-8924 (2017) doi: 10.1039/c7tb02484c.

45 Zhao, B. & Tan, Z. A. Fluorescent carbon dots: fantastic electroluminescent materials for light-emitting diodes. *Advanced Science* **8**, 2001977 (2021) doi: 10.1002/advs.202001977.

46 Zu, F. L. et al. The quenching of the fluorescence of carbon dots: a review on mechanisms and applications. *Microchimica Acta* **184**, 1899-1914 (2017) doi: 10.1007/s00604-017-2318-9.

47 Chen, Y. H. et al. A self-quenching-resistant carbon-dot powder with tunable solid-state fluorescence and construction of dual-fluorescence morphologies for white light-emission. *Advanced Materials* **28**, 312-318 (2016) doi: 10.1002/adma.201503380.

48 Chen, J. et al. Red-emissive carbon dots for fingerprints detection by spray method: coffee ring effect and unquenched fluorescence in drying process. *ACS Applied Materials & Interfaces* **9**, 18429-18433 (2017) doi: 10.1021/acsami.7b03917.

49 Zhou, D. et al. Conquering aggregation-induced solid-state luminescence quenching of carbon dots through a carbon dots-triggered silica gelation process. *Chemistry of Materials* **29**, 1779-1787 (2017) doi: 10.1021/acs.chemmater.6b05375.

50 Pei, R. F. et al. Light on multi-mode optical properties of carbon dots through rational surface engineering tuning strategies. *Chemical Engineering Journal* **484**, 149459 (2024) doi: 10.1016/j.cej.2024.149459.

51 Wang, H. et al. Photoluminescence enhancement of carbon dots

induced by hybrids of photonic crystals and gold-silver alloy nanoparticles. *Journal of Materials Chemistry C* **6**, 147-152 (2018) doi: 10.1039/c7tc04824f.

52 Murphy, A. et al. Fabrication and optical properties of large-scale arrays of gold nanocavities based on rod-in-a-tube coaxials. *Applied Physics Letters* **102**, 103103 (2013) doi: 10.1063/1.4794935.

53 Law, M. et al. Nanowire dye-sensitized solar cells. *Nature Materials* **4**, 455-459 (2005) doi: 10.1038/nmat1387.

54 Kondratev, V. M. et al. Silicon nanowire-based room-temperature multi-environment ammonia detection. *ACS Applied Nano Materials* **5**, 9940-9949 (2022)

55 Kuznetsov, A. et al. In-plane directional $MoS_2$ emitter employing dielectric nanowire cavity. *Small Structures* **6**, 2400476 (2025) doi: 10.1002/sstr.202400476.

56 Quan, L. N. et al. Nanowires for photonics. *Chemical Reviews* **119**, 9153-9169 (2019) doi: 10.1021/acs.chemrev.9b00240.

57 Kuznetsov, A. et al. Elastic gallium phosphide nanowire optical waveguides—versatile subwavelength platform for integrated photonics. *Small* **19**, 2301660 (2023) doi: 10.1002/smll.202301660.

58 Gridchin, V. O. et al. Selective area epitaxy of GaN nanowires on Si substrates using microsphere lithography: experiment and theory. *Nanomaterials* **12**, 2341 (2022) doi: 10.3390/nano12142341.

59 Guo, W. et al. Catalyst-free InGaN/GaN nanowire light emitting diodes grown on (001) silicon by molecular beam epitaxy. *Nano Letters* **10**, 3355–3359 (2010) doi: 10.1021/nl101027x.

60 Anikina, M. A. et al. Numerical study of GaP nanowires: individual and coupled optical waveguides and resonant phenomena. *Nanomaterials* **13**, 56 (2023) doi: 10.3390/nano13010056.

61 Kuznetsov, A. et al. Anisotropic radiation in heterostructured “emitter in a cavity” nanowire. *Nanomaterials* **12**, 241 (2022)

62 Kondratev, V. M. et al. Si nanowire-based schottky sensors for selective

sensing of $NH_3$ and HCl via impedance spectroscopy. *ACS Applied Nano Materials* **6**, 11513-11523 (2023)

63 Vyacheslavova, E. A. et al. Study of cryogenic unmasked etching of “black silicon” with Ar gas additives. *ACS Omega* **7**, 6053-6057 (2022) doi: 10.1021/acsomega.1c06435.

64 Stepanova, M. et al. Carbon dot films with efficient interdot förster resonance energy transfer for optical coding by ultraviolet photooxidation. *The Journal of Physical Chemistry C* **126**, 10441-10448 (2022) doi: 10.1021/acs.jpcc.2c01736.

65 Nenashev, G. V. et al. Effect of carbon dots concentration on electrical and optical properties of their composites with a conducting polymer. *Molecules* **27**, 8000 (2022) doi: 10.3390/molecules27228000.

66 Barhum, H. et al. Gilded vaterite particles: synthesis, optical characterization, and label-free imaging. *Chemical Engineering Journal* **497**, 154714 (2024) doi: 10.1016/j.cej.2024.154714.

67 Tarsa, E. J. et al. Homoepitaxial growth of GaN under Ga-stable and N-stable conditions by plasma-assisted molecular beam epitaxy. *Journal of Applied Physics* **82**, 5472-5479 (1997) doi: 10.1063/1.365575.

68 Barhum, H. et al. Multicolor phenylenediamine carbon dots for metal-ion detection with picomolar sensitivity. *ACS Applied Nano Materials* **4**, 9919-9931 (2021) doi: 10.1021/acsanm.1c02496.

69 Siampour, H. et al. Observation of large spontaneous emission rate enhancement of quantum dots in a broken-symmetry slow-light waveguide. *npj Quantum Information* **9**, 15 (2013) doi: 10.1038/s41534-023-00686-9.

70 Schneider, P. I. et al. Numerical optimization of the extraction efficiency of a quantum-dot based single-photon emitter into a single-mode fiber. *Optics Express* **26**, 8479-8492 (2018) doi: 10.1364/oe.26.008479.

71 Bertness, K. A. et al. Controlled nucleation of GaN nanowires grown with molecular beam epitaxy. *Advanced Functional Materials* **20**, 2911-2915 (2010) doi: 10.1002/adfm.201000381.

72 Bolshakov, A. D. et al. Theoretical modeling of the self-catalyzed

nanowire growth: nucleation- and adsorption-limited regimes. *Materials Research Express* **4**, 125027 (2017) doi: 10.1088/2053-1591/aa9e9d.

73 Ishizaka, A. & Shiraki, Y. Low temperature surface cleaning of silicon and its application to silicon MBE. *Journal of The Electrochemical Society* **133**, 666 (1986) doi: 10.1149/1.2108651.

74 Kern, W. Evolution of silicon wafer cleaning technology. *Journal of the Electrochemical Society* **137**, 1887 (1990) doi: 10.1149/1.2086825.

75 Fedorov, V. V. et al. Tailoring morphology and vertical yield of self-catalyzed gap nanowires on template-free Si substrates. *Nanomaterials* **11**, 1949 (2021) doi: 10.3390/nano11081949.

76 Cansizoglu, H. et al. Investigation of physical vapor deposition techniques of conformal shell coating for core/shell structures by Monte Carlo simulations. *Thin Solid Films* **583**, 122-128 (2015) doi: 10.1016/j.tsf.2015.03.071.